Supporting Information

Fornito et al. 10.1073/pnas.1204185109

SI Text

S.1. Experimental Paradigm. The task comprised five study and five test phases. Only test phases were scanned. Each study phase comprised 32 trials, where participants were presented with a cue saying either SUBJECT or EXPERIMENTER. After 500 ms, either a word pair (e.g., bacon and eggs; perceive condition) or the first word of a pair and a question mark (bacon and ?; imagine condition) appeared. If the cue read SUBJECT, the participant had to either read the presented word pair aloud (perceive condition) or imagine the second word pair and say the word pair out loud (imagine condition). If the cue read EXPERIMENTER, the experimenter performed the task and read the word pair aloud over the scanner intercom. The subject/experimenter and perceive/imagine conditions were crossed in a 2×2 factorial design.

Test phases, which were scanned, consisted of five sessions, comprising eight blocks of four trials each. Each block was preceded by an instruction presented for 2–8 s indicating the type of judgment required (Fig. S1). A single, centrally presented word was then shown, and participants were required to recollect the context in which the second word in the pair had been presented based on the instruction cue (i.e., did you perceive or imagine it or did you or the experimenter read it?). Participants had 4.5 s to make their response. The semantic baseline asked participants to judge whether a nonstudied word referred to a manmade or naturally occurring object. Blocks alternated between contextual memory and semantic baseline in an $A_1A_2BBA_1A_2BB$ format, where A_1 and A_2 refer to the different types of recollection judgments (i.e., perceived/imagined or self/experimenter). The presentation order of the recollection blocks was counterbalanced across subjects. The intertrial interval was jittered between 500 and 1,400 ms according to an exponential distribution. Responses were made using a button box. When making a response, participants held down the button to indicate their confidence in the response. A confidence bar at the bottom of the screen increased in size to indicate their confidence level. Additional details can be found in ref. 1.

S.2. Image Acquisition, Preprocessing, and General Linear Modeling. Echo planar functional images were acquired using a 3T Siemens TIM Trio system (36 sequential 2-mm-thick axial slices with 1 mm interslice gap oriented ~10–20° to the anterior commissure–posterior commissure (AC-PC) transverse plane and with a time-to-repetition (TR) = 2.25 s and time-to-echo (TE) = 30 ms) across five sessions (200 volumes per session). The first five volumes were discarded to allow for T1 equilibration.

Images were preprocessed and analyzed using SPM5 (http://www.fil.ion.ucl.ac.uk/spm/software/). Functional images were first corrected for head motion and slice-timing differences. The mean of these functional images was coregistered to each participant's T1-weighted image. These T1 images were also segmented into gray, white, and cerebrospinal fluid tissue compartments and spatially normalized to Montreal Neurological Institute stereotaxic space. The realigned, slice time-corrected functional volumes were then spatially realigned using the T1-weighted normalization parameters and resampled in 3-mm^3 voxels. The functional data were spatially smoothed with an 8-mm full-width, half-maximum isotropic Gaussian kernel, temporally filtered (high-pass cutoff of 1/128 Hz) and corrected for temporal autocorrelation using an autoregressive AR (1) model. All image processing and subsequent analyses were performed using Matlab 7.8 (Mathworks).

Task-evoked activity was characterized using a general linear model (GLM) in which the onsets of each event were modeled with zero-duration δ-functions convolved with a canonical hemodynamic response function. Unique covariates modeled the onsets of each correctly responded recollection trial (i.e., perceive/imagine and self/experiment) and their corresponding baseline conditions and instruction periods. A separate regressor modeling incorrectly responded trials was included along with the time and dispersion derivatives of each covariate. Model parameter values were computed by restricted maximum likelihood estimation (additional details in ref. 1). Contrasts between these parameter estimates were used to isolate task-related interactions between networks and brain regions. Although self/experimenter and perceive/imagine recollection trials were modeled separately, the major task-related influence on network activity involved the distinction between semantic baseline and recollection (irrespective of the type of recollection) (Fig. 1). Thus, for simplicity, we focused our analysis on this contrast and collapsed across self/experimenter and perceive/imagine recollection judgments.

S.3. Independent Component Analysis. *Component identification.* We used spatial independent component analysis (ICA) to identify spatially independent, temporally coherent networks of voxels in the functional data. Spatial ICA is a widely used method for decomposing high-dimensional functional MRI (fMRI) data into distinct signal and noise components (2–4), and it has been applied to consistently identify the default mode network (DMN) and different external attention system (EAS) components across diverse experimental paradigms (5–8). A particular advantage of this method is that it makes no a priori assumptions concerning the nature of blood oxygenation level-dependent (BOLD) responses evoked by the task (i.e., it is completely data-driven). This property was desirable for present purposes given variability and contradictions concerning how the EAS should be best defined. For example, ICA consistently identifies the cinguloopercular network (CON) as distinct from the dorsal attention network (DAN) and frontoparietal systems (6, 9), whereas seed-based correlation approaches typically include these networks in one unitary system (10). The differences between the two techniques arise because seed-based techniques identify regions showing strong functional connectivity with the seed region alone, whereas ICA identifies regions making a strong contribution to the network as a whole, while also maximizing spatial independence between components. This property of ICA ensured that our network definitions were not biased by a priori selection of specific seed regions and allowed a finer-grained analysis of the specificity of interactions between the DMN and different EAS components. Examining this specificity is critical given metaanalytic evidence for functional dissociations between EAS components (6, 11). Functional dissociations between EAS components were also evident in our findings.

Spatial ICA was implemented using the Group ICA for fMRI Toolbox (http://mialab.mrn.org/software/gift/). Briefly, the analysis proceeded in three broad stages. The dimensionality of the data was reduced from 195 (the number of time points per session) to 21 components through a two-step principle components analysis and subjectwise data concatenation procedure. The dimensionality of the data (number of components) was determined by information theoretic criteria (12). A group spatial ICA was then performed on the concatenated and reduced data using the Infomax algorithm. Spatial maps and representative time courses of each component were subsequently estimated for each subject through back-reconstruction, allowing representation

of interindividual variation in component anatomy and temporal dynamics. The resulting output was a series of spatial maps and representative time courses for each subject, each session, and each of the 21 estimated components. Both spatial maps and time courses were calibrated using z scores. As such, voxel intensities in the spatial maps encoded the degree to which that voxel's activity time course was coherent with the overall component time course; the units in the time course reflected moment-to-moment fluctuations in component activity relative to the session mean. Detailed descriptions of the methods have been provided elsewhere (2).

Spatial mapping. The spatial anatomy of each component was characterized by entering the participant-specific spatial maps into a second-level, one-sample t test to identify voxels with group-averaged z scores that were significantly different from zero. The threshold for significance was set using a familywise error rate correction procedure as implemented in SPM5 ($P < 0.05$, cluster extent = 10 voxels). These spatial maps were in combination with the unthresholded component maps and time courses to identify the DMN, CON, DAN, left frontoparietal network (LFPN), and right frontoparietal network (RFPN) based on their known functional anatomy and comparisons with prior literature (10, 11, 13–15). These five networks could be clearly differentiated from other components reflecting signal and noise in the data.

Task-related modulation of component time courses. To understand how activity in the DMN, CON, DAN, LFPN, and RFPN was modulated by the task, each network's time course was regressed against covariates modeling condition-specific activity defined in the GLM activation analysis (*SI Text, section S.2*). The result was a series of β-coefficients quantifying the degree to which each network's activity covaried with each task condition. To isolate task-related modulations of network activity specific to contextual recollection, we compared the magnitude of these β-coefficients for recollection trials (collapsed across perceive/imagine and self/experimenter conditions) with the corresponding coefficients for semantic baseline trials using one-way ANOVA. As reported in the text, this analysis revealed that activity was significantly greater in recollection than baseline trials in the four EAS components, whereas DMN activity was greater for baseline compared with recollection trials.

S.4. Network Interaction Analysis. Functional interactions between the DMN, DAN, CON, LFPN, and RFPN were characterized using functional connectivity analysis. Functional connectivity refers to a statistical dependence between spatially distinct neurophysiological signals (16). In our analyses, this dependence was computed using partial correlations between network time courses, as described below. These analyses were performed separately to estimate task-unrelated and task-related functional interactions between networks. This distinction is critical, because correlations between raw time courses measured during task-based fMRI can arise for a number of reasons. Primary among these reasons are task-unrelated, spontaneous, or intrinsic functional dynamics; task-related, context-dependent modulations of functional coupling; physiological and/or scanner noise; and interregional coactivation induced by the task, which can arise from independent task-related regional activation in the absence of direct functional interaction. Our analyses aimed to separate task-related and task-unrelated components of functional interactions between networks, while controlling for noise-related effects and coactivation.

Measuring task-unrelated network interactions. Spontaneous fluctuations of the BOLD signal recorded in the absence of an explicit task are highly organized, showing temporal coherence across spatially distributed and well-characterized functional networks of brain regions (17). These correlations persist during task performance (18), account for a major source of variance in task-evoked activity (19–21), and are under strong genetic influence (22, 23). Thus, these task-unrelated processes putatively reflect intrinsic interregional synchronization dynamics (17).

We used previously described and validated methods to isolate task-unrelated interactions between the DMN and the four EAS networks. Specifically, for each participant, each of the five network time courses of interest was band pass-filtered ($0.008 < f < 0.08$) to remove very low-frequency confounds, high-frequency physiological noise and isolate the low-frequency fluctuations known to dominate spontaneous BOLD signals (24). These temporally filtered time courses were then orthogonalized with respect to the following variables: (*i*) six head motion parameters (three translation and three rotation parameters) estimated during motion correction of the functional volumes; (*ii*) signal time courses extracted from spherical seed regions placed in the cerebrospinal fluid (CSF) and white matter; (*iii*) a mean signal extracted from a mask of the entire cerebrum; and (*iv*) all task regressors (including time and dispersion derivatives) included in the GLM as well as additional regressors modeling sustained activity across each task block.

The temporal filtering and correction for head motion, white matter, CSF, and global signals emulate preprocessing strategies traditionally used in analyses of spontaneous BOLD signal correlations (25). These methods are routinely used to investigate anticorrelated interactions between large-scale brain networks (5, 26, 27). Orthogonalization with respect to the task design matrix removed as much task-related variance from the network time courses as possible. Functional connectivity measures derived from the residuals of this correction process have been shown to yield results comparable with those findings obtained using task-free, resting-state fMRI data (28), and the method has been used to link individual differences in task performance to putative anticorrelated spontaneous dynamics recorded during the task (5).

Network interactions were estimated as the partial correlation between each subject's noise- and task-corrected DMN time course, t_{DMN}, and each of the four noise- and task-corrected EAS network time courses, t_{EAS_i}, while controlling for the effects of the remaining three networks [i.e., $r_{t_{DMN},t_{EAS_i},t_{EAS}\setminus\{t_{EAS_i}\}}$, where $t_{EAS} = \{t_{\mathrm{CON}}, t_{\mathrm{DAN}}, t_{\mathrm{LFPN}}, t_{\mathrm{RFPN}}\}$]. This procedure allowed us to isolate functional interactions that were specific to each DMN and EAS component pair.

Orthogonalizing fMRI time series with respect to task design matrices has often been used to approximate task-unrelated functional processes that putatively reflect intrinsic neural dynamics during task performance (5, 28). We preferred this method to using a pure resting-state design because we wanted to examine these processes during performance of the actual task and not during a completely different psychological context and experimental preparation. This choice is justified by recent evidence indicating that psychological context can indeed influence functional connectivity measures obtained during resting-state recordings (29–31). It is important to note that although the correction procedure described above is able to reproduce functional networks observed during resting-state designs with high fidelity, some differences can be apparent and possibly reflect residual, unmodeled task-related variance in the data (28). In our analyses, a failure to adequately remove task-related activity would increase the similarity between task-unrelated and task-related network interaction measures and reduce our power to detect differences between the two. As such, our findings may represent a conservative estimate of the true variation between task-related and task-unrelated functional dynamics.

Measuring task-related, context-dependent network interactions. Task-related functional connectivity describes interregional interactions that vary in accordance with changing task conditions (i.e., interactions that change from one task condition to the next). As such, they reflect interregional synchronization dynamics specifically associated with the cognitive operation(s) being probed

by the experimental task. It is important, however, to distinguish these context-dependent effects from task-unrelated, spontaneous processes and coactivation effects. The latter may arise simply because task stimulation drives activity in two different regions in a similar way, causing their time courses to be correlated even if the regions do not directly interact with each other (i.e., the two regions activate independently to the task).

To isolate task-related network interactions while controlling for such effects, we implemented a correlational technique based on the logic of psychophysiological interactions (PPI) (32). In a traditional PPI analysis, a representative activity time course of a seed region, t, is extracted and multiplied by a task regressor of interest, ψ, to generate a term reflecting the psychophysiological interaction between the seed region's activity and the specified experimental manipulation. Voxels showing significant covariations with the seed region's task-related activity are then identified using a GLM of the form (Eq. **S1**)

$$y_i = I_j \cdot \beta_i + \left[t_j \psi \mathcal{G}\right] \cdot \beta_G + e_i, \qquad \textbf{[S1]}$$

where y_i denotes the activity in voxel i, $I_j = t_j \times \psi$ (the PPI term for seed time course t_j), $\mathcal{G}$ denotes a matrix with columns that contain covariates of no interest, and e_i represents experimental error. The coefficient β_i is the parameter estimate for the PPI term I_j, and β_G represents the parameter estimates for the main effects t_j, ψ, and $\mathcal{G}$. Including the main effect of t_j in the model controls for task-unrelated covariance between t_j and y_i and/or any noise-related processes correlated with t_j. Including the main effect of ψ in the model controls for possible coactivation effects induced by the task waveform. Thus, the model isolates context-sensitive alterations in functional coupling, while controlling for task-unrelated functional connectivity, noise, and coactivation effects.

The model defined in Eq. **S1** is inherently directional; i.e., for any given pair of time series, one must be designated as the predictor and the other must be designated the response variable. The analysis therefore provides a rudimentary model of effective connectivity (32) and works well when there are clear hypotheses about which region might be driving activity in other areas. However, in cases where no such predictions can be made, the assignment of one or the other time course to the left- or right-hand side of Eq. **S1** can be arbitrary.

To avoid arbitrary directional assumptions and retain a focus on analysis of functional rather than effective connectivity between networks, we used a partial correlation framework to estimate task-related, pairwise interactions between the DMN and the four EAS networks. Specifically, for each pair of networks, we generated two PPI terms, I_{DMN} and I_{EAS_i}, by separately multiplying the task regressor ψ with the two network time courses t_{DMN} and t_{EAS_i}, respectively. We then computed the partial correlation $r_{I_{DMN},I_{EAS_i}\cdot Z}$, where $Z = \{t_{DMN}, t_{EAS}, \psi\}$. This correlational PPI (cPPI) approach thus quantifies covariations in task-related activity modulations of the DMN and each EAS network (the PPI terms I_{DMN} and I_{EAS_i}), while controlling for background fluctuations (and correlated noise processes) in the activity of the DMN and all four EAS networks (t_{DMN} and t_{EAS}), as well as any coactivation effects induced by the task stimulation (ψ). In our analyses, our task regressor modeled activity modulations that were greater during recollection than semantic baseline trials, consistent with our interest in this particular task manipulation.

When computing the interaction term I for each time series, we used the deconvolution approach advocated in ref. 33. Specifically, we used an empirical Bayesian method for hemodynamic deconvolution of the original BOLD time series, t, to estimate underlying neuronal activity. This estimated neural signal was then multiplied by the unconvolved task regressor and reconvolved to generate a BOLD-level measurement of the neural PPI term. Computing the PPI interaction term with signals already convolved with a hemodynamic response function is not equivalent to the hemodynamic convolution of an interaction computed at the neural level [i.e., $(H\psi)(Ht) \neq H(\psi t)$, where H is the hemodynamic response function in Toeplitz matrix form]. The deconvolution step therefore provides a more direct estimate of interactions between neural activity and the task, because such interactions occur at the neural rather than hemodynamic level (additional details in ref. 30). Software for implementing cPPI analysis is freely downloadable at http://www.psychiatry.unimelb.edu.au/centres-units/mnc/research/connectivity_software.html.

Addressing motion and other confounds. In our analyses, we accounted for the potential effects of head motion and other confounds by analyzing the residuals obtained after regressing our signals of interest against time courses representing these noise effects, consistent with widely used protocols (17). Recent work has suggested that such an approach may not be sufficient to remove all noise-related effects from the data (34, 35). Residual noise effects are unlikely to impact our findings for several reasons.

First, our main finding, that recollection reaction time (RT) is correlated with DMN–RFPN ni_t and not ni_s values, persisted after we corrected for time courses extracted from all other components identified in the ICA. These components represent a variety of sources of both neural signal and noise, including complex head motion and physiological artifacts (36). Thus, these effects cannot explain the observed brain–behavior associations.

Second, our analyses were focused on examining differences between task-related and task-unrelated components of network interactions within the same individual and dataset. Thus, any contributions of head motion or physiological noise to these data will be equivalent and subtract out in any comparisons.

Third, we reanalyzed the data after controlling for several additional parameters describing various head motion properties. Specifically, we computed the number of significant movements (defined as >0.10 mm relative displacement between adjacent volumes), mean head displacement, maximum head displacement, and mean head rotation, as described in ref. 34. The association between DMN–RFPN ni_t and RT values actually strengthened ($\rho = -0.771, P = 0.005$), whereas the association between RT and ni_s was virtually unchanged ($\rho = -0.353, P = 0.26$).

S.5. Modularity Analysis. We used graph theoretic techniques (37, 38) and modularity analysis (39–41) to characterize, in more detail, the roles that individual brain regions played in facilitating functional interactions between the DMN and RFPN. For each participant, we modeled interactions between regions comprising the DMN and RFPN as a weighted, unthresholded graph of 34 nodes connected by all possible $(34^2 - 34)/2 = 561$ edges. In all graphs, the nodes represented the different brain regions constituting each network (20 DMN and 14 RFPN regions), and they were defined by generating 4-mm-radius spheres centered on the stereotactic coordinates of each significant cluster maximum and submaxima in the statistically thresholded component spatial maps (Fig. 2 *A* and *E* and Table S2). Two separate graphs were constructed for each participant, representing task-unrelated and task-related interactions between regions, as estimated using the methods described above.

Participant-specific modular decomposition. Modularity detection algorithms enable a data-driven partition of a graph-based representation of network connectivity into subgroups of nodes, termed modules, which show higher connectivity with each other than with other areas. Identifying the optimal modular decomposition of a graph is a rich field of inquiry within complex network science, and many alternative algorithms are available (reviewed in ref. 42). Typically, these algorithms attempt to maximize some quality function reflecting the goodness of the partition. Most commonly, this function reflects the difference between the degree of observed intramodular connectivity and the degree expected by chance (40). In our analysis, we used a

generalization of this definition applicable to unthresholded, weighted, and signed graphs (39), where the goodness of the partition was given by (Eq. **S2**)

$$Q^{*} = \frac{1}{v^{+}} \sum_{ij} \left(w_{ij}^{+} - e_{ij}^{+} \right) \delta_{M_i M_j} - \frac{1}{v^{+} + v^{-}} \sum_{ij} \left(w_{ij}^{-} - e_{ij}^{-} \right) \delta_{M_i M_j}. \quad \textbf{[S2]}$$

In this formulation, w_{ij}^{+} and w_{ij}^{-} reflect the positive and negative connection strengths between nodes i and j, respectively, and $\delta_{M_i M_j} = 1$ if nodes i and j belong to the same module, M ($\delta_{M_i M_j} = 0$ otherwise). The chance-expected positive connectivity between nodes i and j is given by $e_{ij}^{+} = \frac{s_i^{+} s_j^{+}}{v^{+}}$, where s^{+} reflects the sum of each node's positive weights and v^{+} reflects the sum total of positive weights in the graph. Similarly, the chance-expected negative connectivity between nodes i and j is given by $e_{ij}^{-} = \frac{s_i^{-} s_j^{-}}{v^{-}}$. The factor $\frac{1}{v^{+}}$ rescales the contribution of positive within-module connectivity to the range [0, 1]. The factor $\frac{1}{v^{+}+v^{-}}$ rescales the contribution of negative within-module connectivity in the same range, while also down-weighting the contribution of negative relative to positive weights in the final estimation of network modularity, Q^{*}. This asymmetric weighting is applied, because positively weighted connectivity directly associates nodes with a given module (i.e., high positive connectivity between nodes implies that they serve similar functions and should be assigned to the same module), whereas negative connection weights indirectly associate nodes with modules by dissociating them from other nodes (i.e., high negative connectivity between nodes implies that they serve opposing functions and should be placed in distinct modules, although a specific modular identity is not necessarily assigned; additional details in ref. 39). By this formulation, a graph partition maximizing Q^{*} will be one with high positive and low negative intramodular connectivity between nodes. We used the Louvain method (43) to find partitions optimizing Q^{*}, as implemented in freely available software (https://sites.google.com/a/brain-connectivity-toolbox.net/bct/).

Determining the optimal modular decomposition of a graph is a nontrivial (nondeterministic, polynomial-time hard) problem, and heuristics are often used to estimate the optimum solution (42). As a result, severe degeneracies in the final solution can arise; i.e., the final decomposition may represent one example of a range of alternative partitions with comparable goodness-of-fit estimates (44). To account for any potential degeneracies in our data, we iterated the algorithm 10,000 times for each dataset. Across these iterations, the number of unique partitions found was generally very low. For the task-related connectivity networks, the mode percentage of degenerate partitions found across participants was <0.01%, and the maximum was 1.4%; for the task-unrelated connectivity networks, the mode was <0.01%, and the maximum was 1.5%. For all datasets, the most frequently found partition was the partition with the maximal Q^{*} value. These data strongly suggest that this partition represented the optimum modular decomposition for each dataset.

Group-level representation of modular architecture. Due to intersubject variability in brain network organization, the brain's modular structure will vary from person to person. Identifying which nodes are consistently coclassified into the same module and which nodes show a more variable pattern of module membership, therefore, represents a critical step in understanding conservation and variability of brain functional organization across subjects. To this end, we adapted previously described methods (45) to derive a group-level characterization of modular architecture. Specifically, we took the optimal modular decomposition for each subject identified in the degeneracy analysis described above and constructed a 34×34 coclassification matrix, such that $C_{ij} = 1$ if nodes i and j belonged to the same module and $C_{ij} = 0$ otherwise. We then summed these matrices across subjects to generate a group consistency matrix, G. The weights of this consistency matrix, G_{ij}, reflected the number of participants for whom nodes i and j were classified in the same module (Fig. 2 *B* and *F*).

The consistency matrix G was then subjected to a further modular decomposition. Thus, nodes that were frequently coclassified in the same module across participants were more likely to belong to the same module in the decomposition of G. We iterated the algorithm 10,000 times to test for degeneracies in the data, although these degeneracies were extremely low (<0.01% for the task-related data and 0 for the task-unrelated data), providing confidence in the robustness of the findings. The resulting partition associated with the highest Q^{*} value was taken as the optimum modular architecture representative of the entire sample (Fig. 2 *B*, *C*, *F*, and *G*).

Node roles. We characterized the roles of each individual node using cartographic analysis of the modular decomposition of G (39, 41, 46). In such an analysis, the role that each node plays within the wider network can be characterized using two measures: the within-module strength, z, and the diversity coefficient, h. The within-module strength quantifies each node's intramodular connectivity. Formally (Eq. **S3**),

$$z = \frac{s_i(m_i) - \bar{s}(m_i)}{\sigma^{s(m_i)}}, \quad \textbf{[S3]}$$

where m_i is the module containing node i, $s_i(m_i)$ is the intramodule nodal strength of node i, defined as the sum of the within-module weights of node i, and $\bar{s}(m_i)$ and $\sigma^{s(m_i)}$ are the mean and SD of the intramodule strength of all nodes in module m_i, respectively.

The diversity coefficient can be used to characterize how each node's connectivity is distributed across different modules, and it is computed as (Eq. **S4**)

$$h_i = \frac{1}{\log m} \sum_{u \in M} p_i(u) \log p_i(u), \quad \textbf{[S4]}$$

where $p_i(u) = \frac{s_i(u)}{s_i}$, $s_i(u)$ is the strength of node i in module u, and m is the number of modules in the partition M.

In typical applications, nodes with high z are interpreted to represent local, intramodular information-processing hubs, whereas nodes with high h show a relatively even distribution of connectivity across all modules (i.e., they support functional integration between modules). In our analyses, we computed these measures using edge weights derived from the group consistency matrix, G. The weights in G do not reflect a direct measure of connectivity between nodes but rather, the frequency with which two nodes were coclassified into the same module across subjects. Thus, nodes with high z in our application showed high classification consistency (i.e., a high probability of being coclassified with other nodes in the same module relative to the other nodes). Regions with high z scores therefore represent a core element of the module to which they belong, showing a relatively conserved modular identity across subjects. Because of their conserved nature, these modules are also likely to represent connectivity hubs within their module. Nodes with high h showed high classification diversity; i.e., they showed a more equal probability of being coclassified with nodes assigned to different modules because their modular identity was variable from person to person. Thus, these regions retained high levels of connectivity with nodes assigned to diverse modules across participants, consistent with a role in facilitating functional integration between modules.

We focused our analysis of node roles on the group consistency matrix data rather than individual differences in participant-specific values, because the number of modules found from subject

to subject was variable. This variability can influence resulting network measures. The best way of accounting for such variability is unclear (preliminary work in this area is in ref. 47).

S.6. Analysis of Brain–Behavior Correlations. Associations between network interaction values and behavioral performance during recollection trials were computed using Spearman's rank correlation. The significance of each observed association was tested against an empirical null distribution obtained by 5,000 permutations of the data. To control type I error rates, correlations were declared significant only if they survived a Bonferroni correction of $\alpha = 0.05/4 = 0.013$, because interaction values between four network pairs were tested for association with each behavioral measure. Differences between correlation coefficients were tested using the Dunn and Clark statistic, ZI^* (48).

To test for associations between recollection RT and node-specific connectivity measures, we computed, for each participant, the total nodal strength of each of the 34 nodes studied in the modularity analysis (Fig. 2 and Table S2). This measure is a commonly used index of the strength of each node's connectivity with the rest of the network, and it is formally defined as (Eq. **S5**)

$$s_i = \frac{1}{N-1}\sum_{j \in N} w_{ij}, \qquad \textbf{[S5]}$$

where w_{ij} represents the absolute connectivity weight between nodes i and j, and N represents the total number of nodes.

Individual differences in the connectivity strength of each node were correlated with recollection RT using the same procedure described above. No significant associations were found, even when using a relatively liberal threshold of $P < 0.05$, uncorrected. Similarly, no associations were found when using strength measures computed separately for positive and negative connectivity weights. These results suggest that task performance was specifically associated with the large-scale collective dynamics of the DMN and RFPN rather than the contributions of any individual brain region.

S.7. Results. ***Behavioral analysis.*** RTs were significantly slower during recollection (M = 1,730.8 ms; SD = 209.44 ms) than semantic baseline trials [M = 1,090.2 ms; SD = 166.89 ms; t (15) = −15.82, $P < 0.001$], consistent with the greater demand placed on memory retrieval processes during the former condition. The variance in accuracy measures (percentage correct) during baseline trials was not sufficient to allow statistical analysis, because all participants were at ceiling (median = 0.99, interquartile range = 0.02), although it was, on average, higher than in recollection trials (median = 0.83, interquartile range = 0.10).

Individual differences in task-related and task-unrelated network interactions. Fig. S2 illustrates the individual variability of task-unrelated and task-related network interaction estimates for each DMN–EAS component pair. Estimates derived using raw network time courses are presented for comparison (the only processing applied to these data was a high-pass filter with a cutoff at 0.008 Hz to remove low-frequency noise). As can be seen, functional interactions between the DMN and each EAS component varied considerably across individuals and in a network- and context-specific manner.

In general, a range of positive and negative network interactions were observed for functional connectivity between the DMN and CON and DMN and RFPN, indicating that these network pairs interacted competitively for some participants and cooperatively for others. In contrast, there was a strong trend for DMN–LPFN interactions to be cooperative and DMN–DAN interactions to be competitive for most participants. These general trends were, however, modulated by whether the task-unrelated or task-related component of network interactions was being assessed. In particular, both DMN–DAN and DMN–RFPN task-related interaction values, ni_t, were significantly higher than task-unrelated interactions, ni_s. For the DMN–DAN pair, this finding reflected an attenuation of the average degree of anti-correlation apparent in task-unrelated interactions [e.g., median $ni_s = -0.50$; median $ni_t = -0.14$; t (15) = −9.61, $P < 0.001$]. For the DMN–RFPN pair, the sample average functional connectivity shifted from negatively to positively correlated when moving from task-unrelated to task-related estimates [median $ni_s = -0.10$; median $ni_t = 0.11$; t (15) = −5.87, $P < 0.001$]. Although a range of both positive and negative values was observed for both task-unrelated and task-related DMN–RFPN interactions, this shift to more positive ni_t values is consistent with our brain–behavior correlations, suggesting that cooperative, context-dependent interactions between these networks facilitate better task performance.

DMN–CON interactions were relatively constant across task-unrelated and task-related components, suggesting relatively little contextual modulation of functional interactions between these networks. On average, interactions between the DMN and LFPN were cooperative, and there was a trend for ni_s to be higher than ni_t values [t (15) = 2.07, P = 0.06). This finding highlights substantial differences in the way in which the left- and right-lateralized aspects of the frontoparietal system interact with the DMN and how these interactions are modulated by task context. This result, combined with our finding of a specific association between DMN–RFPN ni_t values and recollection RT, supports our analysis of the LFPN and RFPN as distinct functional networks.

Collectively, these results highlight three important points: (*i*) there is substantial individual variability in terms of whether any given pair of networks interacts competitively or cooperatively; (*ii*) there is considerable diversity of interactions between the DMN and different components of the EAS; and (*iii*) complete characterization of this diversity requires a distinction between task-related and task-unrelated components of the functional interactions between networks. In particular, interactions between the DMN and DAN and DMN and RFPN showed significant differences in task-related and task-unrelated interaction values, suggesting that functional connectivity between these network pairs was particularly affected by task performance. Reanalysis of the data using nonparametric statistics (Wilcoxon's signed rank test) generally yielded the same results (the only notable variation was that the difference between ni_s and ni_t for DMN–LFPN interactions changed from trend-level to barely significant; i.e., from P = 0.06 to P = 0.049), indicating that outliers or violations of parametric assumptions did not drive the findings.

One concern is that the above differences reflect the global signal correction procedure implemented when estimating task-unrelated network interactions. We used this step to emulate traditional preprocessing strategies in resting-state analyses, but the procedure is known to enhance the degree of anticorrelation between DMN and EAS regions (27, 49). We therefore repeated the analyses using measures of task-unrelated network interactions that were not corrected for the global mean signal (Fig. S3). The results for comparisons between task-related and task-unrelated network interactions were similar; the major variations were that the difference between DMN–RFPN ni_s and ni_t reached significance (P = 0.02), whereas the differences between raw and task-unrelated network interactions for the DMN–DAN and DMN–RFPN pairs were no longer significant (P = 0.08 and P = 0.12, respectively). The correlation between recollection RT and DMN–RFPN ni_s was still not significant when ni_s was estimated without global signal correction. This finding was the case after correcting for covariance with signals from the CON, LFPN, and DAN components ($\rho = -0.42$, P = 0.11) as well as after correcting for covariance with all other components identified in the ICA ($\rho = -0.06$, P = 0.83).

1. Simons JS, Henson RN, Gilbert SJ, Fletcher PC (2008) Separable forms of reality monitoring supported by anterior prefrontal cortex. *J Cogn Neurosci* 20: 447–457.
2. Calhoun VD, Adali T, Pekar JJ (2004) A method for comparing group fMRI data using independent component analysis: Application to visual, motor and visuomotor tasks. *Magn Reson Imaging* 22:1181–1191.
3. Calhoun VD, Kiehl KA, Pearlson GD (2008) Modulation of temporally coherent brain networks estimated using ICA at rest and during cognitive tasks. *Hum Brain Mapp* 29: 828–838.
4. Beckmann CF, Smith SM (2004) Probabilistic independent component analysis for functional magnetic resonance imaging. *IEEE Trans Med Imaging* 23:137–152.
5. Kelly AM, Uddin LQ, Biswal BB, Castellanos FX, Milham MP (2008) Competition between functional brain networks mediates behavioral variability. *Neuroimage* 39: 527–537.
6. Smith SM, et al. (2009) Correspondence of the brain's functional architecture during activation and rest. *Proc Natl Acad Sci USA* 106:13040–13045.
7. Eichele T, et al. (2008) Prediction of human errors by maladaptive changes in event-related brain networks. *Proc Natl Acad Sci USA* 105:6173–6178.
8. Leech R, Kamourieh S, Beckmann CF, Sharp DJ (2011) Fractionating the default mode network: Distinct contributions of the ventral and dorsal posterior cingulate cortex to cognitive control. *J Neurosci* 31:3217–3224.
9. Seeley WW, et al. (2007) Dissociable intrinsic connectivity networks for salience processing and executive control. *J Neurosci* 27:2349–2356.
10. Vincent JL, Kahn I, Snyder AZ, Raichle ME, Buckner RL (2008) Evidence for a frontoparietal control system revealed by intrinsic functional connectivity. *J Neurophysiol* 100:3328–3342.
11. Dosenbach NU, et al. (2006) A core system for the implementation of task sets. *Neuron* 50:799–812.
12. Li YO, Adali T, Calhoun VD (2007) Estimating the number of independent components for functional magnetic resonance imaging data. *Hum Brain Mapp* 28: 1251–1266.
13. Harrison BJ, et al. (2008) Consistency and functional specialization in the default mode brain network. *Proc Natl Acad Sci USA* 105:9781–9786.
14. Smith EE, Jonides J, Marshuetz C, Koeppe RA (1998) Components of verbal working memory: Evidence from neuroimaging. *Proc Natl Acad Sci USA* 95:876–882.
15. Damoiseaux JS, et al. (2006) Consistent resting-state networks across healthy subjects. *Proc Natl Acad Sci USA* 103:13848–13853.
16. Friston KJ (1994) Functional and effective connectivity in neuroimaging: A synthesis. *Hum Brain Mapp* 2:56–78.
17. Fox MD, Raichle ME (2007) Spontaneous fluctuations in brain activity observed with functional magnetic resonance imaging. *Nat Rev Neurosci* 8:700–711.
18. Fransson P (2006) How default is the default mode of brain function? Further evidence from intrinsic BOLD signal fluctuations. *Neuropsychologia* 44:2836–2845.
19. Fox MD, Snyder AZ, Vincent JL, Raichle ME (2007) Intrinsic fluctuations within cortical systems account for intertrial variability in human behavior. *Neuron* 56:171–184.
20. Fox MD, Snyder AZ, Zacks JM, Raichle ME (2006) Coherent spontaneous activity accounts for trial-to-trial variability in human evoked brain responses. *Nat Neurosci* 9: 23–25.
21. Hesselmann G, Kell CA, Eger E, Kleinschmidt A (2008) Spontaneous local variations in ongoing neural activity bias perceptual decisions. *Proc Natl Acad Sci USA* 105: 10984–10989.
22. Fornito A, et al. (2011) Genetic influences on cost-efficient organization of human cortical functional networks. *J Neurosci* 31:3261–3270.
23. Glahn DC, et al. (2010) Genetic control over the resting brain. *Proc Natl Acad Sci USA* 107:1223–1228.
24. Cordes D, et al. (2001) Frequencies contributing to functional connectivity in the cerebral cortex in "resting-state" data. *AJNR Am J Neuroradiol* 22:1326–1333.
25. Van Dijk KR, et al. (2010) Intrinsic functional connectivity as a tool for human connectomics: Theory, properties, and optimization. *J Neurophysiol* 103:297–321.
26. Fox MD, et al. (2005) The human brain is intrinsically organized into dynamic, anticorrelated functional networks. *Proc Natl Acad Sci USA* 102:9673–9678.
27. Fox MD, Zhang D, Snyder AZ, Raichle ME (2009) The global signal and observed anticorrelated resting state brain networks. *J Neurophysiol* 101:3270–3283.
28. Fair DA, et al. (2007) A method for using blocked and event-related fMRI data to study "resting state" functional connectivity. *Neuroimage* 35:396–405.
29. Barnes A, Bullmore ET, Suckling J (2009) Endogenous human brain dynamics recover slowly following cognitive effort. *PLoS One* 4:e6626.
30. Harrison BJ, et al. (2008) Modulation of brain resting-state networks by sad mood induction. *PLoS One* 3:e1794.
31. Lewis CM, Baldassarre A, Committeri G, Romani GL, Corbetta M (2009) Learning sculpts the spontaneous activity of the resting human brain. *Proc Natl Acad Sci USA* 106:17558–17563.
32. Friston KJ, et al. (1997) Psychophysiological and modulatory interactions in neuroimaging. *Neuroimage* 6:218–229.
33. Gitelman DR, Penny WD, Ashburner J, Friston KJ (2003) Modeling regional and psychophysiologic interactions in fMRI: The importance of hemodynamic deconvolution. *Neuroimage* 19:200–207.
34. Van Dijk KR, Sabuncu MR, Buckner RL (2012) The influence of head motion on intrinsic functional connectivity MRI. *Neuroimage* 59:431–438.
35. Power JD, Barnes KA, Snyder AZ, Schlaggar BL, Petersen SE (2012) Spurious but systematic correlations in functional connectivity MRI networks arise from subject motion. *Neuroimage* 59:2142–2154.
36. Beckmann CF, DeLuca M, Devlin JT, Smith SM (2005) Investigations into resting-state connectivity using independent component analysis. *Philos Trans R Soc Lond B Biol Sci* 360:1001–1013.
37. Rubinov M, Sporns O (2010) Complex network measures of brain connectivity: Uses and interpretations. *Neuroimage* 52:1059–1069.
38. Bullmore E, Sporns O (2009) Complex brain networks: Graph theoretical analysis of structural and functional systems. *Nat Rev Neurosci* 10:186–198.
39. Rubinov M, Sporns O (2011) Weight-conserving characterization of complex functional brain networks. *Neuroimage* 56:2068–2079.
40. Newman ME, Girvan M (2004) Finding and evaluating community structure in networks. *Phys Rev E Stat Nonlin Soft Matter Phys* 69:026113.
41. Guimerà R, Nunes Amaral LA (2005) Functional cartography of complex metabolic networks. *Nature* 433:895–900.
42. Fortunato S (2010) Community detection in graphs. *Phys Rep* 486:75–174.
43. Blondel VD, Guillaume J-L, Lambiotte R, Lefebvre E (2008) Fast unfolding of communities in large networks. *J Stat Mech-Theory E*, 10.1088/1742-5468/2008/10/P1008.
44. Good BH, de Montjoye YA, Clauset A (2010) Performance of modularity maximization in practical contexts. *Phys Rev E Stat Nonlin Soft Matter Phys* 81:046106.
45. van den Heuvel M, Mandl R, Hulshoff Pol H (2008) Normalized cut group clustering of resting-state FMRI data. *PloS One* 3:e2001.
46. Meunier D, Achard S, Morcom A, Bullmore E (2009) Age-related changes in modular organization of human brain functional networks. *Neuroimage* 44:715–723.
47. Alexander-Bloch A, et al. (2012) The discovery of population differences in network community structure: New methods and applications to brain functional networks in schizophrenia. *Neuroimage* 59:3889–3900.
48. Steiger JH (2005) Comparing correlations: Pattern hypothesis tests between and/or withing independent samples. *Contemporary Psychometrics: A Festschrift for Roderick P. McDonald*, eds Maydeu-Olivares A, McArdle J (Lawrence Erlbaum Associates Publishers, Mahwah, NJ), pp 377–414.
49. Murphy K, Birn RM, Handwerker DA, Jones TB, Bandettini PA (2009) The impact of global signal regression on resting state correlations: Are anti-correlated networks introduced? *Neuroimage* 44:893–905.

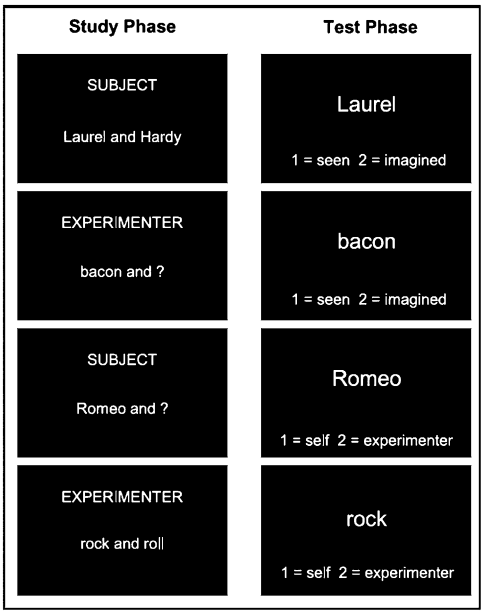

Fig. S1. Example of task stimuli used during the study (*Left*) and test (*Right*) phases. [Reproduced with permission from ref. 1 (Copyright 2008, MIT Press Journals).]

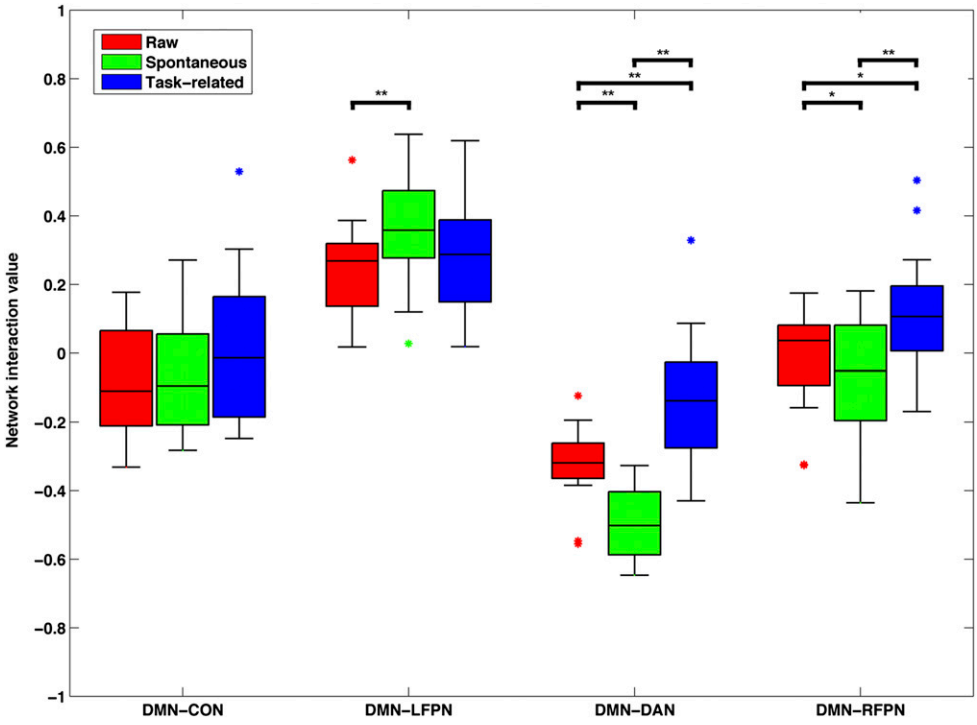

Fig. S2. Box-and-whisker plots illustrating the range of network interaction values observed for each network pair computed using raw network time courses (red), the task-unrelated, putative spontaneous component of these time courses (green), or the task-related component (blue). The central lines in each box represent the sample median, and the boxes represent the interquartile range. Whiskers mark the 5th and 95th percentiles; colored asterisks indicate values beyond this range. Thick horizontal lines indicate differences significant at $P \leq 0.05$. *$P \leq 0.01$; **$P \leq 0.001$. CON, cinguloopercular network; DAN, dorsal attention network; DMN, default mode network; LFPN, left frontoparietal network; RFPN, right frontoparietal network.

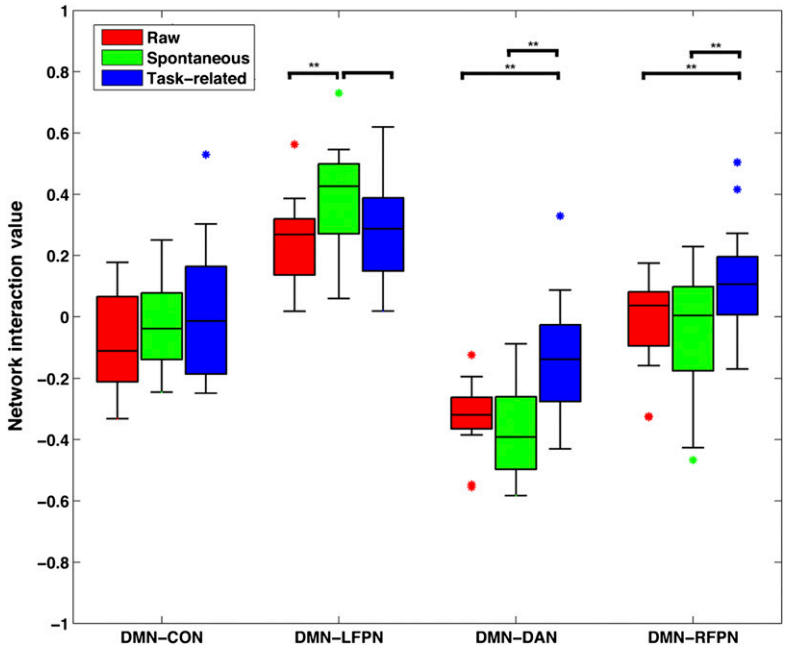

Fig. S3. Box-and-whisker plots illustrating differences between raw, task-related, and task-unrelated (putative spontaneous) network interaction values, where task-unrelated interaction values have been estimated without global signal correction (raw and task-related interaction values remain unchanged from Fig. S2). The central lines in each box represent the sample median, and the boxes represent the interquartile range. Whiskers mark the 5th and 95th percentiles; colored asterisks indicate values beyond this range. Thick horizontal lines indicate differences significant at $P \leq 0.05$. $^{**}P \leq 0.001$. CON, cinguloopercular network; DAN, dorsal attention network; DMN, default mode network; LFPN, left frontoparietal network; RFPN, right frontoparietal network.

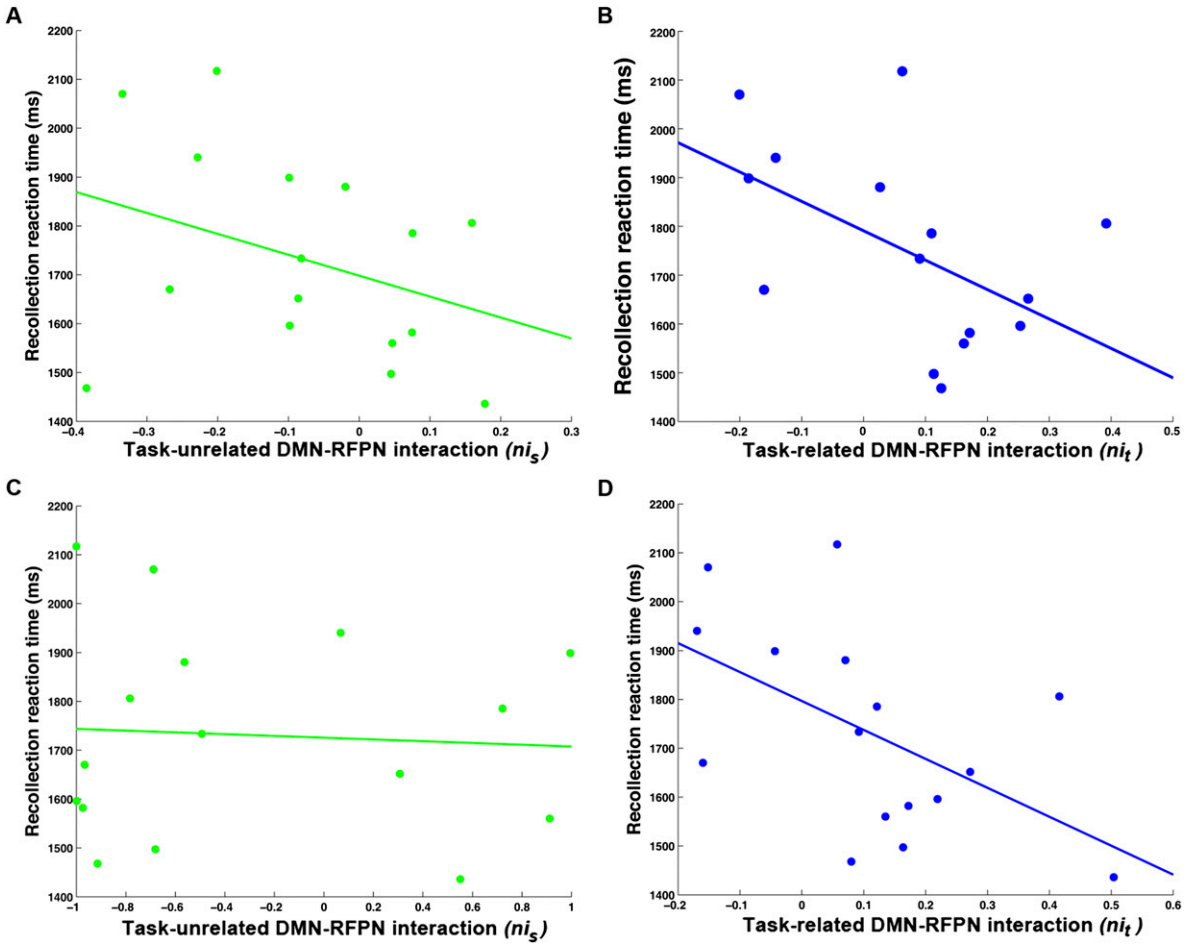

Fig. S4. Scatterplots of the association between recollection RT and DMN–RFPN interaction values. *A* shows the association between RT and task-unrelated interaction values computed after correcting for covariance with signals from the CON, DAN, and LFPN components. *B* shows the association between RT and task-related interaction values corrected in the same way. *C* and *D* show the associations between RT and task-unrelated and task-related interaction values, respectively, after correcting for covariance with signals from all other components estimated in the ICA.

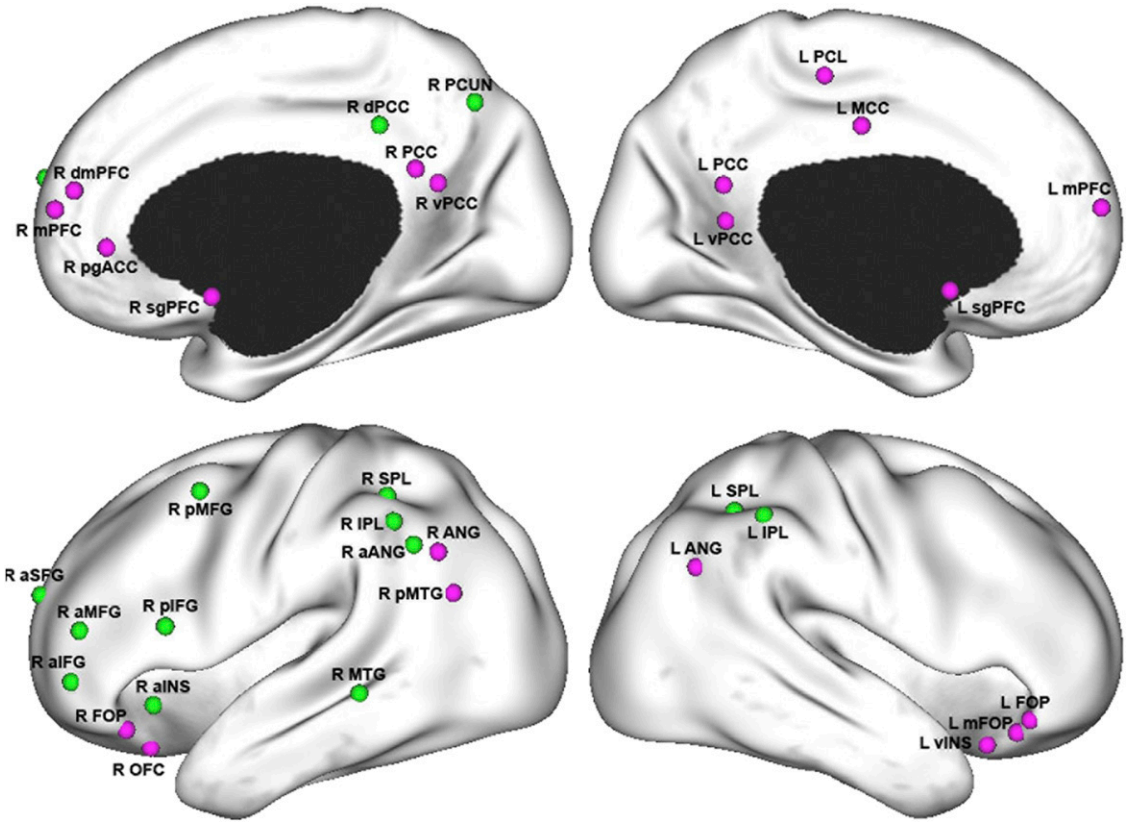

Fig. S5. Anatomical location of spherical regions of interest comprising the DMN (magenta) and RFPN (green) components as identified by the ICA.

Table S1. Regions showing significant group-averaged functional connectivity within each ICA component

Region	*x*	*y*	*z*	Size (voxels)	*Z*
CON					
L anterior insula	36	12	−3	443	7.59
R dorsal anterior cingulate cortex	3	33	27	1,188	7.40
R anterior insula	−45	12	−6	530	6.35
R midbrain	−3	−18	3	245	6.23
R caudate	15	9	15	70	6.05
L midcingulate cortex	−6	−21	33	60	5.79
R middle frontal gyrus	30	51	18	25	5.61
L precentral sulcus	−39	−3	51	25	5.35
L middle frontal gyrus	−30	51	24	40	5.22
R precentral sulcus	33	−3	54	10	5.15
DAN					
L intraparietal sulcus	−27	−69	39	1,093	7.30
R intraparietal sulcus	33	−45	48	926	6.72
R posterior superior temporal sulcus	51	−42	15	18	5.89
L frontal eye fields	−48	6	30	39	5.72
L dorsal precentral sulcus	−27	−6	63	30	5.50
L cuneus	−12	−102	3	11	5.22
LFPN					
L intraparietal lobule	−45	−66	39	818	7.19
L middle temporal gyrus	−60	−45	−6	264	6.90
L inferior frontal gyrus	−48	18	24	871	6.58
L dorsomedial prefrontal cortex	−6	36	42	267	6.45
L precuneus	−3	−63	39	29	6.00
L frontal operculum	−36	18	−18	10	5.48
L precuneus	−9	−45	39	12	5.46
RFPN					
R intraparietal lobule	54	−45	45	804	7.48
R precuneus	6	−72	48	72	6.92
R inferior frontal gyrus	36	48	−3	845	6.52
L superior parietal lobule	−39	−51	48	65	6.02
R anterior insula	39	24	−6	19	5.66
R dorsal posterior cingulate cortex	6	−39	39	34	5.56
R middle temporal gyurs	63	−36	−6	21	5.52
R inferior frontal gyrus	54	21	15	10	5.50
R middle frontal gyrus	21	57	24	13	5.32
DMN					
Anterior medial prefrontal cortex	0	63	15	2,378	>9
R posterior cingulate cortex	3	−51	27	234	6.75
L midcingulate cortex	−3	−18	39	65	6.38
R angular gyrus	54	−57	36	79	6.17
L angular gyrus	−45	−57	33	84	6
L frontal operculum	−36	27	−15	35	5.54
R frontal operculum	42	27	−15	32	5.46

CON, cinguloopercular network; DAN, dorsal attention network; DMN, default mode network; L, left hemisphere; LFPN, left frontoparietal network; R, right hemisphere; RFPN, right frontoparietal network.

Table S2. Names and coordinates of regions of interest studied in the modularity analysis

Region	Abbreviation*	*x*	*y*	*z*
RFPN				
L superior parietal lobule	L SPL	−39	−51	48
L inferior parietal lobule	L IPL	−51	−45	48
R dorsal posterior cingulate cortex	R dPCC	6	−39	39
R precuneus	R PCUN	6	−72	48
R anterior superior frontal gyrus	R aSFG	21	57	24
R posterior middle frontal gyrus	R pMFG	36	9	51
R anterior inferior frontal gyrus	R aIFG	36	48	−3
R anterior insula	R aINS	39	24	−6
R anterior middle frontal gyrus	R aMFG	45	45	15
R superior parietal lobule	R SPL	48	−42	51
R anterior angular gyrus	R aANG	51	−51	36
R inferior parietal lobule	R IPL	54	−45	45
R posterior inferior frontal gyrus	R pIFG	54	21	15
R middle temporal gyrus	R MTG	63	−36	−6
DMN				
L posterior cingulate cortex[†]	L PCC	−2	−57	21
L subgenual prefrontal cortex[‡]	L sgPFC	−2	6	−12
L medial prefrontal cortex[§]	L mPFC	−2	63	15
L midcingulate cortex	L MCC	−3	−18	39
L paracentral lobule	L PCL	−3	−30	51
L ventral posterior cingulate cortex	L vPCC	−6	−57	9
L ventral insula	L vINS	−30	18	−15
L middle frontal operculum	L mFOP	−36	27	−15
L angular gyrus	L ANG	−45	−57	33
L frontal operculum	L FOP	−48	27	−12
R ventral posterior cingulate cortex[†]	R vPCC	2	−57	21
R subgenual prefrontal cortex[‡]	R sgPFC	2	6	−12
R medial prefrontal cortex[§]	R mPFC	2	63	15
R posterior cingulate cortex	R PCC	3	−51	27
R pregenual anterior cingulate cortex	R pgACC	3	48	3
R dorsomedial prefrontal cortex	R dmPFC	3	54	21
R orbitofrontal cortex	R OFC	33	21	−21
R frontal operculum	R FOP	42	27	−15
R angular gyrus	R ANG	54	−57	36
R posterior middle temporal gyrus	R pMTG	54	−63	21

DMN, default mode network; L, left hemisphere; R, right hemisphere; RFPN, right frontoparietal network.
*Abbreviations correspond to the region of interest (ROI) abbreviations used in Fig. 2.
[†,‡,§]These regional pairs were created from an original single cluster maximum located at $x = 0$. To avoid generating an ROI centered on the midline, where CSF is prevalent, two ROIs were instead created and symmetrically placed 2 mm from the midline with the same *y* and *z* coordinates.